Complex Organic Molecules in Taurus Molecular Cloud-1

The Astrophysical Journal, 854:116 (11pp), 2018 February 20 https://doi.org/10.3847/1538-4357/aaa70c

Complex Organic Molecules in Taurus Molecular Cloud-1

Tatsuya Soma[1], Nami Sakai[2], Yoshimasa Watanabe[1,3,4], and Satoshi Yamamoto[1]
[1] Department of Physics, The University of Tokyo Bunkyo-ku, Tokyo 113-0033, Japan
[2] The Institute of Physical and Chemical Research (RIKEN), Wako, Saitama 351-0198, Japan; nami.sakai@riken.jp
[3] Division of Physics, Faculty of Pure and Applied Sciences, University of Tsukuba, Tsukuba, Ibaraki 305-8571, Japan
[4] Tomonaga Center for the History of the Universe, University of Tsukuba, Tsukuba, Ibaraki 305-8571, Japan
Received 2016 November 24; revised 2017 December 26; accepted 2018 January 8; published 2018 February 16

Abstract

We have observed the millimeter-wave rotational spectral lines of CH_3CHO, H_2CCO, cyclopropenone, and H_2CO toward the cyanoployyne peak of Taurus Molecular Cloud-1 (TMC-1 CP). The spectral line profile of CH_3CHO is found to reveal a well-separated double peak. It is similar to the line profile of CH_3OH, but is much different from those of carbon-chain molecules and $C^{34}S$. The different line profiles mean different distributions along the line of sight. The similarity of the spectral line profiles between CH_3CHO and CH_3OH suggests that CH_3CHO is mainly formed on dust grains as CH_3OH or through gas-phase reactions starting from CH_3OH. On the other hand, the spectral line profiles of H_2CCO and cyclopropenone are rather similar to those of carbon-chain molecules and $C^{34}S$, implying their gas-phase productions. H_2CO shows a composite spectral line profile reflecting the contributions of both gas-phase and grain-surface productions. In addition, we have detected the spectral lines of CH_3CHO and $HCOOCH_3$ toward the methanol peak near TMC-1 CP. We have also tentatively detected one line of $(CH_3)_2O$. Considering the chemical youth of TMC-1, the present results indicate that fairly complex organic species have already been formed in the early evolutionary phase of starless cores. TMC-1 is thus recognized as a novel source where formation processes of complex organic molecules can be studied on the basis of the line profiles.

Key words: ISM: abundances – ISM: individual objects (TMC-1) – ISM: molecules

1. Introduction

Recently, we observed the millimeter-wave rotational emission lines of CH_3OH toward the representative starless core, the cyanopolyyne peak of TMC-1 (referred to hereafter as TMC-1 CP), at high velocity resolution, and found that their spectral line profiles are much different from those of carbon-chain molecules and $C^{34}S$ (Soma et al. 2015). Spectral line profiles of carbon-chain molecules and $C^{34}S$ observed toward TMC-1 CP show complex features reflecting a complex internal structure of the core (e.g., Hirahara et al. 1992; Langer et al. 1995; Dickens et al. 2001). On the other hand, the CH_3OH lines have a double-peaked profile separated by 0.5 km s^{-1}, and its total velocity range is slightly wider than those of carbon-chain molecules and $C^{34}S$. The double-peaked profile is also observed for $^{13}CH_3OH$, indicating that it is not due to the self-absorption effect. The difference of the line profiles mentioned above indicates that the emitting region of CH_3OH is different from that of the other molecules. According to the mapping observations of the CH_3OH and $C^{34}S$ lines, their different distributions have indeed been confirmed. In TMC-1 CP, CH_3OH is preferentially distributed in the less dense ((1–4) $\times$ 10^4 cm^{-3}) gas possibly surrounding the dense core traced by carbon-chain molecules and $C^{34}S$.

Since the gas-phase production of CH_3OH is inefficient (Geppert et al. 2006), CH_3OH is thought to be produced on dust grains through hydrogenation of CO, as confirmed by the laboratory experiment (Watanabe & Kouchi 2002). CH_3OH produced on dust grains seems to be liberated by nonthermal processes, including desorption by surplus reaction energy, desorption by cosmic-ray induced UV radiation, and photodesorption around the cloud peripheries, although it has recently been suggested that the photodesorption of CH_3OH is less efficient than previously thought (Bertin et al. 2016; Martín-Doménech et al. 2016). The grain origin of CH_3OH was recently supported by the measurement of the $^{12}C/^{13}C$ ratio (Soma et al. 2015). In contrast, carbon-chain molecules and CS are thought to be produced in a dense core through gas-phase reactions (e.g., Herbst & Leung 1989; Suzuki et al. 1992; Aikawa et al. 2001; Yamamoto 2017). Since TMC-1 CP has a rather complex internal structure and kinematics as mentioned above, the different distributions of molecules produced in the gas-phase reactions and those liberated from dust grains could be disentangled on the basis of the spectral line profile.

CH_3OH is the most representative saturated organic molecule formed on dust grains. More complex organic molecules (COMs), such as CH_3CHO, $HCOOCH_3$ and $(CH_3)_2O$, would also be produced on dust grains. So far, these molecules are widely detected toward hot cores of high-mass star-forming regions (e.g., Blake et al. 1987; Bisschop et al. 2007), and hot corinos of low-mass star-forming regions (e.g., Cazaux et al. 2003; Bottinelli et al. 2004; Sakai et al. 2006; Imai et al. 2016). In these sources, COMs formed on dust grains are sublimated in a hot region near protostars. In addition, COMs are also detected in the outflow-shocked region L1157 B1, where COMs are liberated into the gas phase by sputtering (Arce et al. 2008; Sugimura et al. 2011). On the other hand, COMs have been detected in relatively cold sources. Although CH_3CHO is detected in various cold sources (e.g., Matthews et al. 1985; Öberg et al. 2010; Vastel et al. 2014; Potapov et al. 2016), the detection of $HCOOCH_3$ and/or $(CH_3)_2O$ has been limited to the two starless cores,

L1689B, and L1544 (Bacmann et al. 2012; Jimenez-Serra et al. 2016) and the cold star-forming core B1b (Öberg et al. 2010; Cernicharo et al. 2012). In the cold sources, COMs would probably be liberated by the nonthermal desorption, as in the case of CH_3OH detected in TMC-1 CP. Alternatively, COMs may be formed through gas-phase reactions starting from CH_3OH (Vasyunin & Herbst 2013; Balucani et al. 2015). The detections of COMs in L1689B and L1544 suggest that more COMs besides CH_3OH could also be found in TMC-1 CP and their line profile would be similar to that observed for CH_3OH. In other words, we can study the formation mechanisms of COMs in TMC-1 CP on the basis of their line profile without extensive mapping observations of the faint lines. Although CH_3CHO was detected in TMC-1 CP (Matthews et al. 1985; Kaifu et al. 2004), its line profile was not well resolved. With these in mind, we conducted sensitive observations of several COMs and their related species at a high velocity resolution.

2. Observations

Observations in the 40 GHz band were carried out with the Robert C. Byrd Green Bank Telescope of the National Radio Astronomy Observatory in 2013 April and 2014 September. We employed the Q-band receiver, whose simultaneous bandwidth is 4 GHz. The system noise temperature typically ranged from 85 to 120 K toward the source. The beam size and the beam efficiency of the telescope were 16″ and 0.70, respectively. The pointing of the telescope was checked by observing the nearby continuum sources every hour, and was maintained to be better than 5″. The frequency-switching mode with a frequency offset of ±2.5 MHz was employed for the observations. The back end was a bank of autocorrelators, whose bandwidth and frequency resolution were 12.5 MHz and 3 kHz, respectively. The frequency resolution corresponds to a velocity resolution of 0.019 km s^{-1} at 47.2 GHz. The intensity scale was calibrated by noise injection.

Observations in the 70 GHz band were conducted with the Nobeyama 45 m telescope. We employed the T70 receiver, whose system noise temperature was 200–300 K depending on the frequency. The beam size and the beam efficiency of the telescope were 20″ and 0.4, respectively. The pointing of the telescope was checked by observing nearby SiO maser source (NML Tau) every hour, and was maintained to be better than 7″. The position-switching mode was used for the observations, where the off-position was taken as $(\alpha_{2000}, \delta_{2000}) = (04^h42^m35\overset{s}{.}92, 25°53'23''.34)$ (Soma et al. 2015). The back end was the autocorrelator SAM45, whose frequency resolution was set to be 30.52 kHz. This frequency resolution corresponds to a velocity resolution of 0.13 km s^{-1} at 70 GHz.

Observations in the 140 GHz band were carried out with the IRAM 30 m telescope at Pico Veleta in 2011 April. The SIS receiver, EMIR, was used as a front end, whose system noise temperature ranged from 100 to 200 K. The beam size and the main beam efficiency of the telescope were 17″ and 0.80 at 145.1 GHz, respectively. The telescope pointing was checked every hour by observing nearby continuum sources, and was maintained to better than 4″. The autocorrelator VESPA was used as a back end. We set the individual bandwidth and resolution to be 20 MHz and 20 kHz, respectively. The frequency resolution corresponds to a velocity resolution of 0.04 km s^{-1} at 140 GHz. The frequency-switching mode was used for the observation.

We observed the spectral lines listed in Table 1 toward TMC-1 CP ($(\alpha_{2000}, \delta_{2000}) = (04^h41^m42\overset{s}{.}88, 25°41'27''.0)$) and the CH_3OH peak of TMC-1 (referred to hereafter as TMC-1 MP). TMC-1 MP is apart from TMC-1 CP by 2′: $(\alpha_{2000}, \delta_{2000}) = (04^h41^m38\overset{s}{.}62, 25°42'09''.8)$. Note that no infrared sources are associated with TMC-1 CP and TMC-1 MP. In all the observations, the two orthogonal polarization signals were averaged to improve the signal-to-noise ratio.

3. Results for TMC-1 CP

We detected the lines of CH_3CHO, H_2CCO, cyclopropenone (c-C_3H_2O), H_2CO, $C^{34}S$, CCS, and HC_7N in our observation. Figure 1 shows the line profiles detected toward TMC-1 CP, which are compared with the CH_3OH line profile. The line parameters are summarized in Table 2. The line profiles of $C^{34}S$, CCS, and HC_7N are narrower than that of CH_3OH, and have complicated velocity structures, as reported by Soma et al. (2015). This indicates that the spatial distributions of $C^{34}S$, CCS, and HC_7N are different from that of CH_3OH. In the following subsections, we describe the result for CH_3CHO, H_2CCO, cyclopropenone, and H_2CO.

3.1. CH_3CHO

Toward TMC-1 CP, we detected the 2_{02}–1_{01}(A and E), and 2_{11}–1_{10} (E) lines of CH_3CHO at 38.5 GHz and 39.4 GHz, respectively. Their spectral line profiles show a well-separated double-peaked structure, and hence, they are fitted to the double-Gaussian function to derive the line parameters for the blueshifted and redshifted components. The results are shown in Table 2. The spectral line profiles are similar to that of CH_3OH, and are different from those of $C^{34}S$, CCS, and HC_7N, as shown in Figure 1. The separation of two peaks of CH_3CHO is 0.49 km s^{-1} on average. The separation is similar to that of CH_3OH (0.46 km s^{-1}), while it is, for example, different from that of HC_7N (0.20 km s^{-1}). On the other hand, the velocity widths of the two components of the double-peaked structure are slightly narrower for CH_3CHO (0.25 km s^{-1} and 0.1 km s^{-1} on average for the red and blueshifted components, respectively) than for CH_3OH (0.30 km s^{-1} and 0.26 km s^{-1} for the red and blueshifted components, respectively). Hence, the emission is very faint at the intermediate velocity around 5.8 km s^{-1} between the two peaks, and thus the two components are well-separated. Regardless of the difference of the line width, similarity of the spectral line shapes between CH_3CHO and CH_3OH indicates their spatial coexistence. We note that the slightly narrower line width of each component for CH_3CHO may mean more compact distribution than that of CH_3OH. The similar line profile to CH_3OH suggests that CH_3CHO is formed on dust grains and is liberated into the gas phase through nonthermal desorption mechanisms as CH_3OH. Alternatively, CH_3CHO may be formed from CH_3OH through gas-phase processes (Johnson et al. 2000).

In TMC-1 CP, CH_3CHO was first detected by Matthews et al. (1985). Kaifu et al. (2004) also detected the CH_3CHO lines in the spectral line survey toward TMC-1 CP. However, the spectral resolution in these observations was not high enough to reveal the above characteristic line profiles, although the observed line widths look slightly broad. The present high spectral resolution observation allowed us to reveal that the line shape of CH_3CHO is different from the rest of the other molecules.

Table 1
Observed Molecular Lines

Molecule	Transition	Frequency (MHz)[a]	E_{up} (K)	$S_{ij}\mu^2$(Debye^2)	Observations[b]
H_2CO[c]	1_{01}–0_{00}	72837.948(10)	3.5	5.44	CP
	2_{02}–1_{01}	145602.949(10)	11	10.9	CP
CH_3OH[c]	1_{01}–0_{00} A$^+$	48372.45580(70)	2.3	0.809	CP, MP
	1_{01}–0_{00} E	48376.892(10)	15[d]	0.808	MP
H_2CCO[c]	2_{02}–1_{01}	40417.950(30)	2.9	4.03	MP
	4_{04}–3_{03}	80832.117(20)	9.7	8.06	CP
	4_{13}–3_{12}	81586.230(20)	23	22.7	CP
CH_3CHO[e]	2_{02}–1_{01} E	38506.0348(13)	2.9	11.7	CP
	2_{02}–1_{01} A	38512.0786(13)	2.8	11.7	CP
	2_{11}–1_{10} E	39362.5367(16)	5.2	8.81	CP, MP
$HCOOCH_3$[e]	4_{04}–3_{03} E	47534.093(50)	5.8	10.5	MP
	4_{04}–3_{03} A	47536.915(50)	5.8	10.5	MP
	4_{14}–3_{13} E	45395.795(50)	6.1	9.95	MP
	4_{14}–3_{13} A	45397.380(50)	6.1	9.95	MP
$(CH_3)_2O$[e]	1_{11} – 0_{00} EE	47674.9576(47)	2.3	27.1	MP
	5_{14}–5_{05} EE	39047.303(30)	15	128	CP
c-C_3H_2O (Cyclopropenone)[c]	3_{13}–2_{12}	39956.700(30)	5.0	154	CP
$C^{34}S$[c]	1 – 0	48206.9411(20)	2.3	3.83	CP, MP
	2 – 1	96412.9495(22)	6.9	7.67	CP
CCS[c]	3_3–2_2	38866.4200(25)	12	1.34	CP, MP
HC_5N[c]	18 – 17	47927.27460(20)	22	337	MP
HC_7N[c]	41 – 40	46246.9780(11)	47	953	CP

Notes.
[a] The error denotes one standard deviation in units of the last significant digits.
[b] Observed position: CP; Cyanopolyyne peak: MP; Methanol peak. See the text.
[c] Taken from CDMS (Müller et al. 2005).
[d] Measured from the 0_{00} level of the A state. E_{up} is 7.5 K, if it is measured from the lowest E state (1_{-11}).
[e] Taken from JPL (http://spec.jpl.nasa.gov/ftp/pub/catalog/catdir.html).

3.2. H_2CCO and Cyclopropenone

In grain-surface chemistry, it is proposed that CH_3CHO is formed as an intermediate species during sequential hydrogenation of H_2CCO: $H_2CCO \rightarrow H_3CCO \rightarrow CH_3CHO \rightarrow C_2H_5O \rightarrow C_2H_5OH$ (e.g., Herbst & van Dishoeck 2009). If this mechanism is the case, H_2CCO should also exist on dust grains as a parent molecule forming CH_3CHO. With this in mind, we also observed H_2CCO in TMC-1 CP.

We detected the 4_{04}–3_{03} (para) and 4_{13}–3_{12} (ortho) lines of H_2CCO in the 81 GHz region. As shown in Figure 1, the spectral line profile of H_2CCO looks slightly different from those of CH_3OH and CH_3CHO. Although it shows a double-peaked structure, the two components are substantially blended. The separation of the two components evaluated by the double Gaussian fitting is 0.37 km s^{-1} for the ortho lines and 0.35 km s^{-1} for the para line. These values are smaller than that of CH_3OH (0.49 km s^{-1}).

The overall line shape is rather similar to those of $C^{34}S$ and CCS, indicating that the distribution of H_2CCO would resemble those of CCS and $C^{34}S$. A similarity of the line shape of H_2CCO to those of $C^{34}S$ and CCS is also confirmed at TMC-1 MP, as described in Section 4.1. CS and CCS are thought to be produced by the gas-phase processes (e.g., Aikawa et al. 2001; Suzuki et al. 1992). Actually, the distribution of $C^{34}S$ is much different from that of the dust-origin species, CH_3OH, as reported in Soma et al. (2015). Hence, these results imply that H_2CCO would also be formed mainly through gas-phase reactions in TMC-1 CP, as Irvine et al. (1989) suggested on the basis of the chemical model calculation by Herbst & Leung (1986).

In addition to H_2CCO, we detected the 3_{13}–2_{12} line of cyclopropenone (c-C_3H_2O). Its spectral line profile is found to be blueshifted by ~0.3 km s^{-1}. This shift corresponds to the frequency shift of 40 kHz, and probably originates from insufficient accuracy of the rest frequency, because the uncertainty of this transition is as large as 30 kHz according to CDMS (Müller et al. 2005). Apart from this overall velocity shift, the spectral line profile of cyclopropenone has three (or more) velocity components and resembles those of $C^{34}S$ and CCS. Hence, its production would not be related directly to CH_3OH and CH_3CHO. According to Herbst & van Dishoeck (2009), this molecule is also thought to be produced on dust grains. However, the observed spectral profile suggests that this molecule is mainly produced through gas-phase processes in TMC-1 CP, as in the case of CS and CCS. Recently, Loison et al. (2016) conducted the survey observations of cyclopropenone and propynal (HCCCHO) toward several starless cores including TMC-1, and argued the gas-phase production of these molecules. Their conclusion is consistent with ours. Since the line profile is complicated, only the integrated intensity is given for the cyclopropenone line in Table 2.

3.3. H_2CO

We observed the 1_{01}–0_{00} and 2_{02}–1_{01} lines of para-H_2CO. Their line profiles are apparently broader than that of HC_7N, as shown in Figure 1. The apparent width of the H_2CO line, especially that of the skirt part, is comparable to that of CH_3OH. On the other hand, two peaks are only marginally separated, and the central dip is not as clear as in the case of CH_3OH. Since the line profile is complicated, only the integrated intensity is given

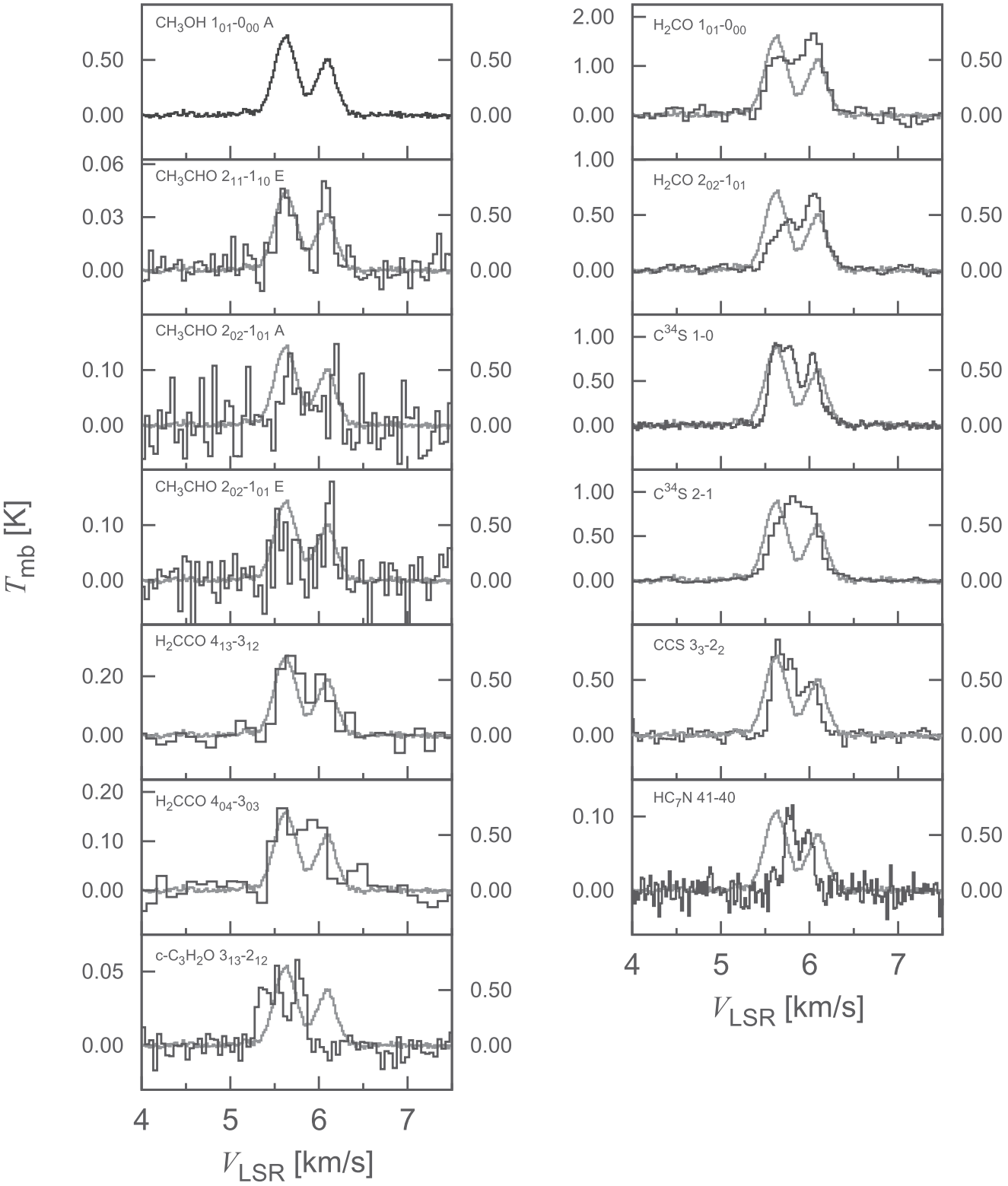

Figure 1. Line profiles observed toward TMC-1 CP. The spectrum of the CH_3OH 1_{01}–0_{00} A^+ line is overlaid on the spectra of the other species (gray). The horizontal bars represent the uncertainties of the rest frequencies.

for the H_2CO lines in Table 2. Relative intensities of the blueshifted and redshifted components are different between the two lines of H_2CO. The blueshifted component is relatively weak in the 2_{02}–1_{01} emission. According to the CH_3OH observation (Soma et al. 2015), the H_2 densities of the blueshifted and redshifted components are $(1.7 \pm 0.5) \times 10^4\,cm^{-3}$ and $(4.3 \pm 1.2) \times 10^4\,cm^{-3}$, respectively. Since the critical densities of the 1_{01}–0_{00} and (2_{02}–1_{01}) lines of H_2CO are $1.5 \times 10^5\,cm^{-3}$ and $5.2 \times 10^5\,cm^{-3}$, respectively, according to the Einstein coefficients and the collisional cross sections

Table 2
Line Parameters toward TMC-1 CP[a]

Molecule	Transition		T_{MB} (K)	ΔV (km s^{-1})	V_{LSR} (km s^{-1})	$\int T_{MB} dv$ (K km s^{-1})	Res.[b] (km s^{-1})	rms[c] (K)
CH_3OH[d]	1_{01}–0_{00} A$^+$	blue	0.702(36)	0.298(3)	5.622(1)	0.365(2)[e]	0.019	0.014
		red	0.491(25)	0.263(4)	6.085(2)			
CH_3CHO[d]	2_{02}–1_{01} E	blue	0.080(24)	0.255(89)	5.607(38)	0.043(8)[e]	0.048	0.042
		red	0.201(47)	0.083(24)	6.128(8)			
	2_{02}–1_{01} A	blue	0.096(27)	0.235(75)	5.691(32)	0.048(7)[e]	0.048	0.035
		red	0.160(46)	0.076(3)	6.188(12)			
	2_{11}–1_{10} E	blue	0.042(5)	0.258(32)	5.636(14)	0.022(1)[e]	0.046	0.006
		red	0.054(7)	0.142(18)	6.079(8)			
$(CH_3)_2O$[f]	5_{14}–5_{05} EE	blue				<0.003		
		red				<0.002		
H_2CO	1_{01}–0_{00}					0.952(21)[g]	0.063	0.106
	2_{02}–1_{01}					0.346(4)[g]	0.040	0.029
c-C_3H_2O	3_{13}–2_{12}					0.022(1)[g]	0.046	0.007
H_2CCO[d]	4_{04}–3_{03}	red	0.151(18)	0.363(84)	5.913(34)	0.104(7)[e]	0.113	0.026
		blue	0.161(27)	0.202(46)	5.567(23)			
	4_{13}–3_{12}	red	0.205(32)	0.197(45)	6.039(20)	0.142(9)[e]	0.112	0.035
		blue	0.290(27)	0.297(40)	5.678(16)			
$C^{34}S$	1–0					0.475(25)[g]	0.019	0.026
	2–1					0.479(3)[g]	0.061	0.023
CCS	3_3–2_2					0.335(13)[g]	0.047	0.085
HC_7N[d]	41–40	red	0.083(8)	0.138(21)	5.981(8)	0.031(1)[e]	0.020	0.015
		blue	0.111(8)	0.143(15)	5.783(6)			

Notes.
[a] The numbers in parentheses represent one standard deviation in units of the last significant digits. The uncertainties for T_{MB}, ΔV, and V_{LSR} are derived from the Gaussian fitting. The uncertainties of the integrated intensities, ΔS, are calculated as $\Delta S = (\Delta T_{MB}/\sqrt{N})\Delta V$, where ΔT_{MB} represents the rms noise per spectral resolution and N the number of spectrum resolution channels over the line width (ΔV).
[b] Velocity resolution of the spectrum shown in Figure 1.
[c] rms noise per spectral resolution shown in Figure 1.
[d] Line parameters are obtained by a Gaussian fit.
[e] Total integrated intensity for the red and blue components.
[f] Lines are not detected. The upper limits correspond to a 3σ detection level. Line widths are estimated by using those of CH_3CHO lines.
[g] Since the line profile is complicated, only the integrated intensity is given.

(LAMDA: Schöier et al. 2005; Wisenfeld & Faure 2013), the two lines are subthermally excited. Hence, the higher excitation line (2_{02}–1_{01}) of H_2CO becomes weaker for the blueshifted component because of the slightly lower H_2 density. The lack of a clear central dip may suggest that the H_2CO lines are optically thick. Alternatively, the dense core component, which is traced by the spectral lines of $C^{34}S$, CCS, and HC_7N, may fill up the dip structure. Actually, the peak positions of the two velocity components coincide with the outer two of the three velocity components in the $C^{34}S$ ($J = 1$–0) and CCS lines. Above all, the spectral line profiles of H_2CO may suggest the mixed characteristics of the gas-phase and dust-grain origins. The partial contribution of the gas-phase production seems reasonable, because H_2CO can be formed, for instance, through ion–molecule reactions such as

$$CH_3^+ + O \rightarrow CH_2O^+ + H \quad (1)$$

$$CH_2O^+ + H_2 \rightarrow CH_2OH^+ + H \quad (2)$$

$$CH_2OH^+ + e^- \rightarrow H_2CO + H. \quad (3)$$

Protonated H_2CO (CH_2OH^+) was recently detected in the starless core L1689B (Bacmann et al. 2016). Its detection in TMC-1 CP will give a constraint on the contribution of the gas-phase production.

4. Results for TMC-1 MP

Following the above results in TMC-1 CP, we searched for more complex organic species such as $HCOOCH_3$ and $(CH_3)_2O$ in TMC-1 MP, because the CH_3OH emission is brighter by a factor of 2 in the CH_3OH peak than in TMC-1 CP. This position is based on the mapping observations of CH_3OH (Soma et al. 2015). As mentioned in Section 2, no infrared source is associated with TMC-1 MP.

The lines observed toward TMC-1 MP are listed in Table 1. We successfully detected the CH_3CHO, H_2CCO, $HCOOCH_3$, and $(CH_3)_2O$ lines in addition to the CH_3OH, $C^{34}S$, CCS, and HC_5N lines. Here the detection of $(CH_3)_2O$ is tentative. Figures 2 and 3 show the line profiles for TMC-1 MP. The line parameters are summarized in Table 3. As in the case of TMC-1 CP, the overall line profiles of $C^{34}S$, CCS, and HC_5N are narrower than that of CH_3OH. The two peaks of the CH_3OH line have a wider separation than the line width of $C^{34}S$, CCS, and HC_5N, the redshifted component being brighter than the blueshifted component. In the following subsections, we describe the results of CH_3CHO, H_2CCO, $HCOOCH_3$, and $(CH_3)_2O$.

4.1. CH_3CHO

Toward TMC-1 MP, we clearly detected the spectral line (2_{11}–1_{10} E) of CH_3CHO. Its spectral line profile is similar to that of the CH_3OH line, but is significantly different from those of

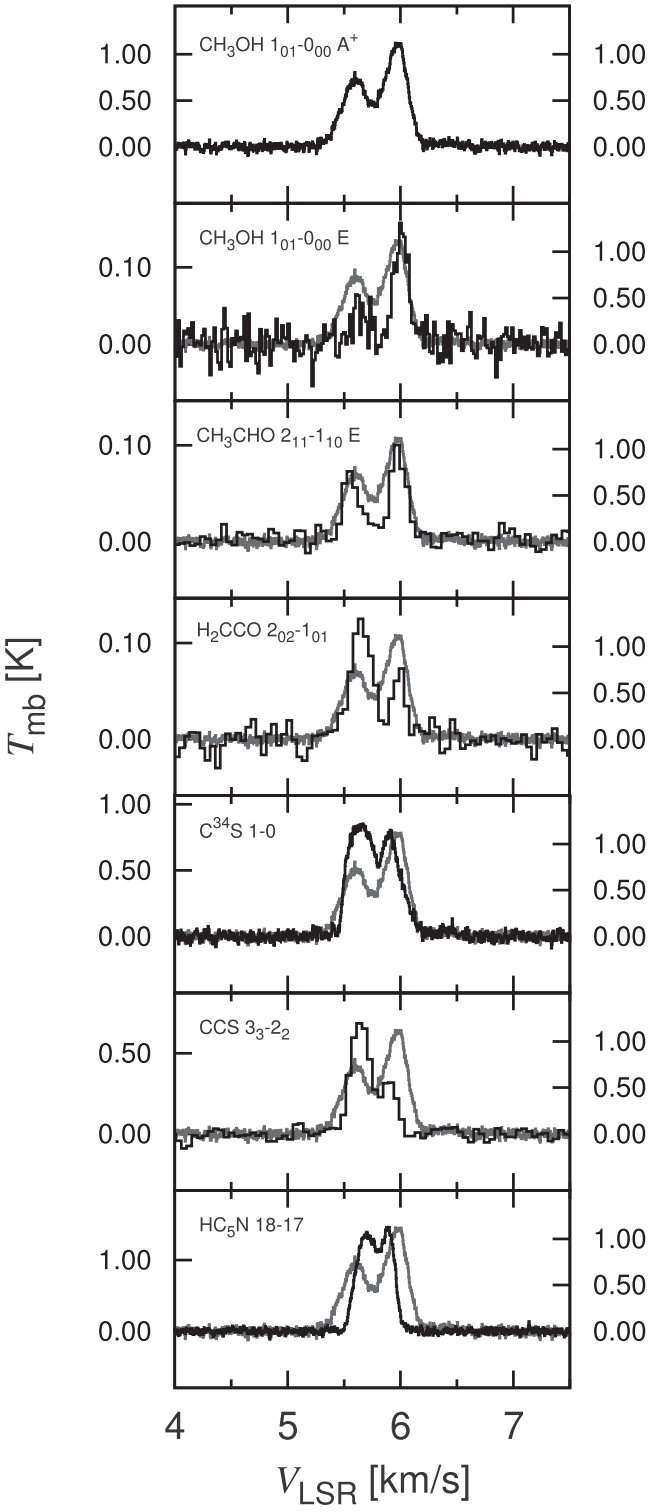

Figure 2. Line profiles observed toward TMC-1 MP. The spectrum of the CH_3OH 1_{01}–0_{00} A^+ line is overlaid on the spectra of the other species (gray). The horizontal bars represent the uncertainties of the rest frequencies.

the CCS and HC_5N lines. The CH_3CHO line is brighter by a factor of 2 than that in TMC-1 CP. As in the case of TMC-1 CP, the velocity widths of the two components (0.20 km s^{-1} and 0.18 km s^{-1} for the red and blueshifted components, respectively) are slightly narrower than those for the CH_3OH A^+ transition (0.30 km s^{-1} and 0.23 km s^{-1} for the red- and blueshifted components, respectively). However, it is comparable to those of the CH_3OH E transition (0.18 km s^{-1} and 0.15 km s^{-1} for the red and blueshifted components, respectively), whose upper state energy is higher than that of the A^+ species. The similarity of the line shapes between CH_3OH and CH_3CHO in TMC-1 MP further suggests the dust-grain origin of these molecules: CH_3CHO is formed on dust grains as in the case of CH_3OH or through gas-phase reactions driven by CH_3OH released from dust grains. The spectral lines are fitted to the double-Gaussian function to obtain the line parameter for the blueshifted and redshifted components separately. The result is shown in Table 3.

4.2. H_2CCO

We detected the H_2CCO line in TMC-1 MP, as in the case of TMC-1 CP. The H_2CCO line shows a double-peaked line profile, where the velocity difference between the two components (0.33 km s^{-1}) is slightly smaller than those for CH_3OH (0.36 km s^{-1} on average) and CH_3CHO (0.41 km s^{-1}). Moreover, the blueshifted component is brighter than the redshifted component for H_2CCO, which is opposite to the CH_3OH and CH_3CHO cases, and is rather similar to the $C^{34}S$ and CCS cases. Although we marginally identify the difference of the line shape between CH_3OH/CH_3CHO and H_2CCO in TMC-1 CP, the difference can be confirmed in TMC-1 MP. Since the line profile of H_2CCO is similar to those of $C^{34}S$ and CCS, the gas-phase reactions seem to play an important role in the production of H_2CCO.

4.3. $HCOOCH_3$ and $(CH_3)_2O$

Since the CH_3CHO line was detected with moderate intensity, we searched for the spectral lines of more complex species, $HCOOCH_3$ and $(CH_3)_2O$, toward TMC-1 MP. As shown in Figure 3, we detected the four lines of $HCOOCH_3$, although each detection is at the (9–15)σ confidence level in integrated intensity ($\int T_{\rm MB} dv$). The line parameters of $HCOOCH_3$ are obtained by the Gaussian fitting, and are summarized in Table 3. The spectral line profiles of the three lines (4_{04}–4_{03} A, 4_{14}–3_{13} A, and 4_{14}–3_{13} E) are similar to one another, where only the redshifted velocity component (~5.9 km s^{-1}) of the double-peaked feature of the CH_3OH lines is seen. Note that the 4_{04}–3_{03} E line has been detected at a slightly different velocity (velocity shift of ~0.15 km s^{-1}). However, the difference (~24 kHz) is smaller than the uncertainty of the rest frequency (50 kHz), and hence the 4_{04}–4_{03} E line is likely detected.

The spectral line profile of $HCOOCH_3$ is peculiar, which only shows the redshifted velocity component out of the two components seen in the CH_3OH and CH_3CHO lines. This result does not necessarily mean that $HCOOCH_3$ preferentially exists in the redshifted component, but may originate from some excitation effects. The redshifted and blueshifted components in TMC-1 MP are physically related to the corresponding redshifted and blueshifted components in TMC-1 CP, respectively (Soma et al. 2015). The redshifted component is denser than the blueshifted component in TMC-1 CP, and this trend is also true in TMC-1 MP, as shown later (Section 4.4). Although the collisional cross sections of this molecule are not available for all the rotational levels, that for the 2_{02} level is reported by Faure et al. (2014). By employing this value, we roughly estimated the critical density of the

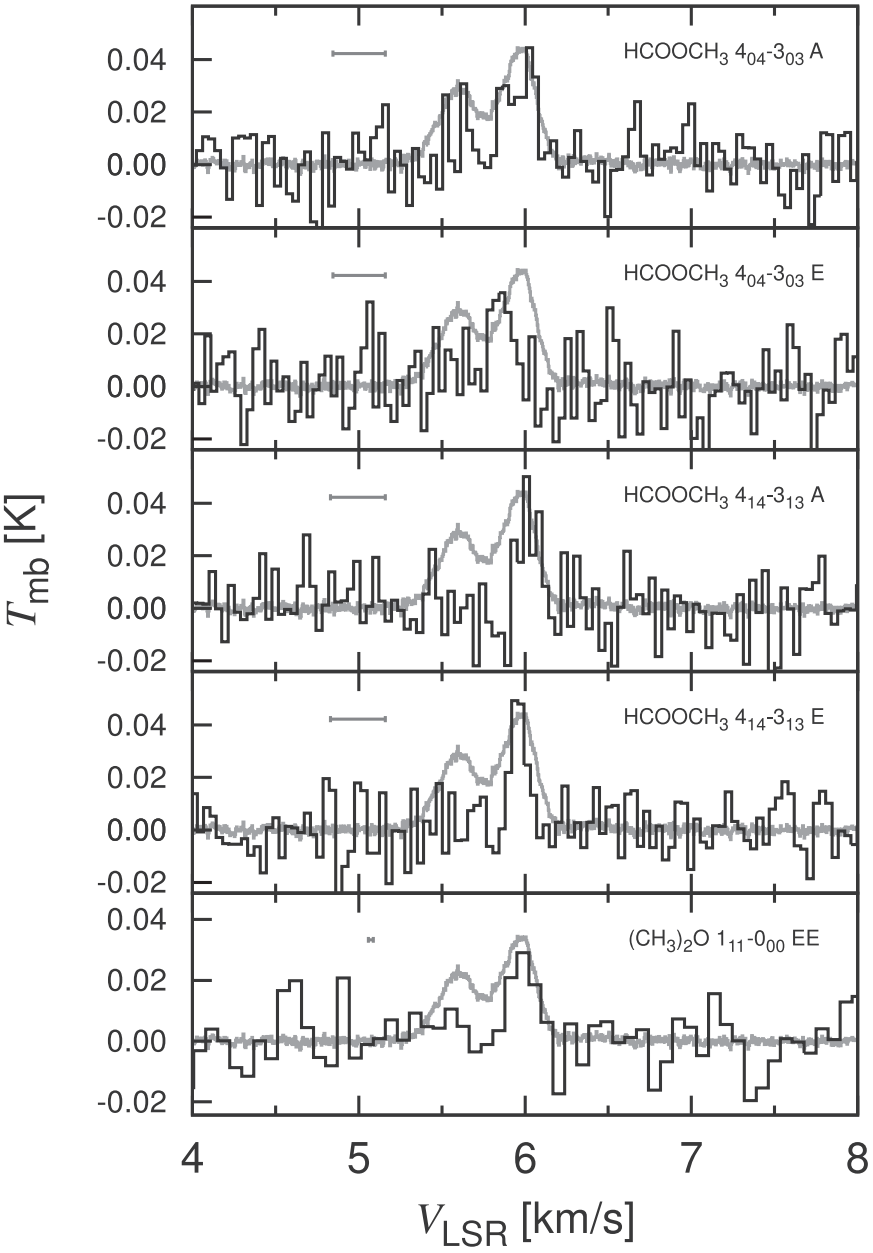

Figure 3. Line profiles of $HCOOCH_3$ and $(CH_3)_2O$ observed toward TMC-1 MP. The spectrum of the CH_3OH 1_{01}–0_{00} A^+ line is overlaid on the spectra of the other species (gray). The horizontal bars represent the uncertainties of the rest frequencies.

observed lines to be $3 \times 10^4\,cm^{-3}$. This value is almost comparable to or higher than the H_2 density of the blueshifted component (see Section 4.4), and hence, only the redshifted component could be detected due to the excitation effect in the limited signal-to-noise ratio. Detection of the three (or possibly four) lines of $HCOOCH_3$ at the velocity of the redshifted velocity component of CH_3OH suggests that $HCOOCH_3$ has the dust-grain origin as in the case of CH_3OH and CH_3CHO.

In addition to $HCOOCH_3$, we tentatively detected the 1_{11}–0_{00} EE line of $(CH_3)_2O$ in TMC-1 MP with the confidence level of 4.8σ in integrated intensity ($\int T_{MB} dv$), as shown in Figure 3. Unfortunately, we observed only one line, because the other internal rotation components of this transition, which fall in the observing band are weaker at least by a factor of 2.7. Hence, we still need confirmation observations to claim definitive detection. Nevertheless, the spectral line profile is similar to that observed for the $HCOOCH_3$ lines: only the redshifted component appears. The line parameters are obtained by the Gaussian fitting and are summarized in Table 3.

Recently, the gas-phase production of the COMs including $HCOOCH_3$ and $(CH_3)_2O$ from CH_3OH are proposed (Vasyunin & Herbst 2013; Balucani et al. 2015). If the liberation of CH_3OH into the gas phase enhances the gas-phase production of the COMs, the similarity of the line shape of CH_3OH with those of $HCOOCH_3$ and $(CH_3)_2O$ for the redshifted component could also be explained. Even in this case, $HCOOCH_3$ and $(CH_3)_2O$ have the dust-grain origin in their production indirectly, which is reflected in their distributions (and in their line shapes).

Table 3
Line Parameters toward TMC-1 MP[a]

Molecule	Transition		T_{MB} (K)	ΔV (km s^{-1})	V_{LSR} (km s^{-1})	$\int T_{MB} dv$ (K km s^{-1})	Res.[b] (km s^{-1})	rms[c] (K)
CH_3OH	1_{01}–0_{00} A$^+$	blue	0.712(6)	0.301(4)	5.604(2)	0.503(2)[d]	0.004	0.030
		red	1.101(6)	0.229(2)	5.967(1)			
	1_{01}–0_{00} E	blue	0.046(6)	0.175(28)	5.641(12)	0.0316(12)[d]	0.018	0.015
		red	0.145(7)	0.154(8)	6.007(4)			
CH_3CHO	2_{11}–1_{10} E	blue	0.097(9)	0.195(21)	5.567(9)	0.034(2)[d]	0.046	0.009
		red	0.136(10)	0.175(14)	5.979(6)			
$HCOOCH_3$	4_{04}–3_{03} A	red	0.030(5)	0.220(46)	5.975(19)	0.0089(8)	0.036	0.009
	4_{04}–3_{03} E	red	0.040(7)	0.123(25)	5.850(10)	0.0055(6)	0.036	0.009
	4_{14}–3_{13} A	red	0.043(6)	0.124(20)	6.029(9)	0.0079(5)	0.038	0.008
	4_{14}–3_{13} E	red	0.059(6)	0.095(12)	5.959(5)	0.0058(4)	0.038	0.007
$(CH_3)_2O$	1_{11}–0_{00} EE	red	0.028(6)	0.184(47)	6.040(20)	0.0053(11)	0.072	0.010
H_2CCO	2_{02}–1_{01}	red	0.073(9)	0.131(19)	5.988(8)	0.0433(15)[d]	0.045	0.010
		blue	0.123(6)	0.226(15)	5.654(6)			
$C^{34}S$	1–0	red	0.707(8)	0.272(7)	5.902(3)	0.4137(11)[d]	0.004	0.030
		blue	0.844(11)	0.223(4)	5.622(2)			
CCS	3_3–2_2	red	0.327(24)	0.151(15)	5.904(6)	0.221(4)[d]	0.047	0.034
		blue	0.714(21)	0.204(9)	5.645(3)			
HC_5N	18–17	red	1.298(13)	0.136(2)	5.897(1)	0.5100(14)[d]	0.004	0.031
		blue	1.400(8)	0.216(3)	5.700(1)			

Notes.
[a] The numbers in parentheses represent one standard deviation in units of the last significant digits. The uncertainties of the integrated intensities, ΔS, are calculated as $\Delta S = (\Delta T_{MB}/\sqrt{N})\Delta V$, where ΔT_{MB} represents the rms noise per spectral resolution and N the number of spectrum resolution channels over the line width (ΔV).
[b] Velocity resolution of the spectrum shown in Figures 2 and 3.
[c] rms noise per spectral resolution shown in Figures 2 and 3.
[d] Total integrated intensity for the red and blue components.

Table 4
Column Densities of CH_3OH, CH_3CHO, and $(CH_3)_2O$ in TMC-1 CP [cm^{-2}]

	Blueshifted Component			Redshifted Component		
Species	T_{rot} = 3.8 K	4.8 K	5.8 K	4.7 K	5.7 K	6.7 K
CH_3OH A[a]		$(1.7 \pm 0.3) \times 10^{13}$			$(9.3 \pm 1.0) \times 10^{12}$	
CH_3OH E[a]		1.5×10^{13}			1.0×10^{13}	
CH_3CHO	$(2.0 \pm 0.3) \times 10^{12}$	$(1.4 \pm 0.3) \times 10^{12}$	$(1.3 \pm 0.2) \times 10^{12}$	$(1.0 \pm 0.2) \times 10^{12}$	$(9.5 \pm 1.7) \times 10^{11}$	$(9.5 \pm 1.7) \times 10^{11}$
$(CH_3)_2O$[b]	$\leqq 1.1 \times 10^{13}$	$\leqq 4.6 \times 10^{12}$	$\leqq 3.0 \times 10^{12}$	$\leqq 3.3 \times 10^{12}$	$\leqq 2.1 \times 10^{12}$	$\leqq 1.6 \times 10^{12}$
H_2CCO[c]	$(1.3 \pm 0.2) \times 10^{13}$	$(6.9 \pm 1.0) \times 10^{12}$	$(5.1 \pm 0.7) \times 10^{12}$	$(4.7 \pm 0.9) \times 10^{12}$	$(3.4 \pm 0.7) \times 10^{12}$	$(2.8 \pm 0.6) \times 10^{12}$

Notes.
[a] Column densities reported by Soma et al. (2015).
[b] The upper limits are derived by the rms noise (3σ).
[c] Blue and redshifted components of this molecule do not exactly correspond to those of CH_3OH and CH_3CHO (see Figure 1 and Section 3.2).

4.4. Physical Conditions of TMC-1 MP

We derive the H_2 density from the 1_{01}–0_{00} A$^+$ and 1_{01}–0_{00} E lines of CH_3OH by using the statistical equilibrium calculation (Goldreich & Kwan 1974). We employ the RADEX code (van der Tak et al. 2007) for this purpose, where the gas kinetic temperature is assumed to be a typical value for starless cores (10 K; e.g., Benson & Myers 1989). We also assume the same abundances of the A and E species of CH_3OH. The H_2 density for the blueshifted and redshifted components are evaluated to be 3.5×10^4 and 1.6×10^5 cm^{-3}, respectively. These H_2 densities are slightly higher than those derived for TMC-1 CP (Soma et al. 2015). The column density of CH_3OH is also derived to be $(2.2 \pm 0.6) \times 10^{13}$ and $(4.0 \pm 1.4) \times 10^{13}$ cm^{-2} for the blueshifted and redshifted components of TMC-1 MP, respectively. The total column density is higher by a factor of 1.5 than that derived toward TMC-1 CP (Soma et al. 2015).

5. Discussions

5.1. Column Densities

The column densities of the detected COMs are derived from the observed intensities by assuming the local thermodynamic equilibrium (LTE) conditions. When the blueshifted and redshifted components are well separated, they are treated individually. Since we observed only one transition or multiple transitions having the similar upper state energies for the most species, we have to assume the excitation temperature.

For CH_3CHO in TMC-1 CP, we employ the LTE excitation temperature for the two velocity components of CH_3OH reported by Soma et al. (2015); T_{ex} is 4.8 K and 5.7 K for the blueshifted and redshifted components, respectively. The results are shown in Table 4. Variations of the column densities by a change in the assumed excitation temperature by ± 1 K are also given in Table 4. The upper limits to the column

Table 5
Column Densities of CH_3CHO, $HCOOCH_3$, $(CH_3)_2O$, and H_2CCO in TMC-1 MP

Species		Column Density (cm^{-2})		
		4.2 K	5.2 K	6.2 K
CH_3CHO	blue	$(2.8 \pm 0.4) \times 10^{12}$	$(2.4 \pm 0.3) \times 10^{12}$	$(2.3 \pm 0.3) \times 10^{12}$
	red	$(3.4 \pm 0.4) \times 10^{12}$	$(3.1 \pm 0.3) \times 10^{12}$	$(3.0 \pm 0.3) \times 10^{12}$
$HCOOCH_3$	red	$(1.9 \pm 0.2) \times 10^{12}$	$(1.6 \pm 0.1) \times 10^{12}$	$(1.5 \pm 0.1) \times 10^{12}$
$(CH_3)_2O$	red	$(2.0 \pm 0.7) \times 10^{12}$	$(1.9 \pm 0.6) \times 10^{12}$	$(2.1 \pm 0.7) \times 10^{12}$
H_2CCO[a]	blue	$(4.8 \pm 0.4) \times 10^{12}$	$(4.0 \pm 0.3) \times 10^{12}$	$(3.7 \pm 0.3) \times 10^{12}$
	red	$(1.6 \pm 0.3) \times 10^{12}$	$(1.4 \pm 0.3) \times 10^{12}$	$(1.3 \pm 0.2) \times 10^{12}$

Note.
[a] Blue and redshifted components of this molecule do not exactly correspond to those of CH_3CHO, $HCOOCH_3$, and $(CH_3)_2O$ (see Figure 2 and Section 4.2). The ortho-to-para ratio is assumed to be 3.

density for $(CH_3)_2O$ in TMC-1CP are calculated in the same way from the root-mean-square noise of the spectrum. We also evaluate the column density of H_2CCO for the blueshifted and redshifted components, assuming the above excitation temperatures. The results are listed in Table 4. However, it should be noted that these two components of H_2CCO do not exactly correspond to those of CH_3OH and CH_3CHO, as mentioned in Section 3.2.

On the other hand, the LTE analysis of H_2CO in TMC-1 CP is unsuccessful, probably because of the subthermal populations and the relatively high optical depths. Hence, we employ the non-LTE code (RADEX) to evaluate the column density of H_2CO. We only evaluate the total column density, because the blueshifted and redshifted components are not well resolved for the H_2CO lines. The column density and the H_2 density are derived to be $1.2 \times 10^{13}\,cm^{-2}$ and $2 \times 10^{4}\,cm^{-3}$, respectively. The line profile is also complicated for cyclopropenone. Hence, only the total column density is derived for this species to be $(5.6 \pm 0.3) \times 10^{11}\,cm^{-2}$ under the assumption of the LTE conditions with the average excitation temperature of the blueshifted and redshifted components of CH_3OH (5.2 K). The column density is $(6.6 \pm 0.3) \times 10^{11}\,cm^{-2}$ and $(5.4 \pm 0.2) \times 10^{11}\,cm^{-2}$, if the excitation temperature is 4.2 and 6.2 K, respectively.

For CH_3CHO, $HCOOCH_3$, and $(CH_3)_2O$ in TMC-1 MP, we derive the column densities by using the average rotation temperature (5.2 K) of the two velocity components of CH_3OH in TMC-1 CP. As in the case of TMC-1 CP, the total column densities for the blueshifted and redshifted components are derived for H_2CCO, although these components would not exactly correspond to those of CH_3CHO, as mentioned in Section 4.1. The results are summarized in Table 5. Variations of the column densities by a change in the assumed rotation temperature by ± 1 K are also shown in Table 5.

5.2. Comparison with other Sources

Although COMs have long been thought to be specific to hot cores in high-mass star-forming regions and hot corinos in low-mass star-forming regions, their existence in cold starless cores has recently been revealed, as mentioned in Section 1. If COMs are produced on dust grains, some desorption mechanisms are necessary for their radio detection in cold starless cores. Desorption by surplus reaction energy, cosmic-ray or cosmic-ray-induced UV radiation, as well as photodesorption by the interstellar UV radiation in cloud peripheries are considered (Bacmann et al. 2012; Caselli et al. 2012), although the photodesorption processes were recently suggested to be less efficient than previously thought (Bertin et al. 2016; Martín-Doménech et al. 2016). Alternatively, the gas-phase formation of COMs is also proposed to account for the result by involving new radiative association reactions (Vasyunin & Herbst 2013; Balucani et al. 2015). Thus, the formation of COMs still remains controversial. However, the similarity of the distribution of COMs and CH_3OH inferred from the similar spectral line shapes in this study favors the dust-grain origin for cold starless cores. At least, the formation of COMs would be triggered by liberation of CH_3OH from dust grain, even if the final production pathways to the COMs are the gas-phase ones.

In this study, we detected CH_3CHO, $HCOOCH_3$, and $(CH_3)_2O$ toward TMC-1 MP, although the detection of $(CH_3)_2O$ is tentative. First, we compare the relative abundances of these three species relative to CH_3OH observed in TMC-1 MP with those in the other cold sources L1544, L1689B, and B1b (Öberg et al. 2010; Bacmann et al. 2012; Jimenez-Serra et al. 2016), as shown in Table 6. Although the ratios are different by a factor of a few among the three sources, we would say in this stage that the relative abundances of these three COMs could be similar to one another among the four sources in a sense of the order-of-magnitude estimate. This result suggests that a common chemistry for the above COMs is occurring in these sources. We need better quality data and their analyses to discuss their source-to-source differences.

In TMC-1 MP, the column density of CH_3CHO is roughly comparable to those of $HCOOCH_3$ and $(CH_3)_2O$. CH_3CHO is often regarded as a "cold molecule," because its excitation temperature is lower than those of hot corino/hot core molecules (Bisschop et al. 2007). Hence, formation processes of CH_3CHO were thought to be different from those of the other COMs. However, the present observation shows on the basis of the spectral line shape that CH_3CHO has the dust-grain origin as in the case of the other COMs for TMC-1 CP and TMC-1 MP.

For comparison with the star-forming regions and the shocked region, we derive the fractional abundances of molecules relative to CH_3OH, as shown in Table 6. In TMC-1 MP, the CH_3CHO/CH_3OH ratio is only lower than that in the hot corino source IRAS 16293-2422 by a factor of 2, while the $HCOOCH_3/CH_3OH$ and $(CH_3)_2O/CH_3OH$ ratios are much lower by one to two orders of magnitude, as shown in Table 6. Larger molecules such as $HCOOCH_3$ and $(CH_3)_2O$ may tend to become abundant during the star formation processes. Garrod & Herbst (2006) proposed that the COMs are formed efficiently on dust grains in warm-up processes during star formation. The observed difference between TMC-1 MP and IRAS

Table 6
Abundance Ratios of COMs Relative to CH_3OH in TMC-1 MP

	TMC-1 MP (blue) (T_{ex} = 5.2 K)	TMC-1 MP (red) (T_{ex} = 5.2 K)	L1544[a,b] (center)	L1544[a,c] (CH_3OH peak)	B1b[d] (Core)	L1689B[e,f] (T_{ex} = 30 K)	L1157[g]	IRAS 16293-2422[h]
CH_3CHO/CH_3OH	0.110 ± 0.034	0.077 ± 0.028	0.04	0.05	0.012 ± 0.002	0.050 ± 0.003	0.0036 ± 0.018	0.17
$HCOOCH_3/CH_3OH$		0.039 ± 0.014	0.16 ± 0.15	0.04 ± 0.02	0.023 ± 0.005	0.084 ± 0.013	0.007 ± 0.003	1.3
CH_3OCH_3/CH_3OH		0.048 ± 0.023	0.056 ± 0.012	0.012 ± 0.002	<0.008	0.084 ± 0.008	<0.005	0.80
$N(CH_3OH)$ [cm^{-2}]	$(2.2 \pm 0.6) \times 10^{13}$	$(4.0 \pm 1.4) \times 10^{13}$	$(2.7 \pm 0.6) \times 10^{13}$	6.3×10^{13}	3.6×10^{13}	1.2×10^{14}	$(6.24 \pm 0.02) \times 10^{15}$	2.25×10^{16}

Notes.
[a] Jimenez-Serra et al. (2016).
[b] Spezzano et al. (2016).
[c] Bizzocchi et al. (2014). The CH_3OH column density is taken from their Figure 3.
[d] Öberg et al. (2010).
[e] Bacmann & Faure (2016).
[f] Bacmann et al. (2016). Column densities for the excitation temperature of 8 K are employed.
[g] Sugimura et al. (2011). Beam averaged values (∼20″).
[h] Cazaux et al. (2003).

16293-2422 may originate from this effect. Alternatively, the difference may reflect the difference of the evaporation mechanism. In the hot corino, the COMs are thought to be thermally evaporated, while in starless cores they come out into the gas phase through nonthermal processes mentioned above. In the former case, all the ice mantles will be evaporated, but not in the letter case. If the ice composition has a layered structure, the different evaporation mechanisms would cause the different gas-phase compositions.

It is interesting to compare the abundances with those in the outflow-shocked region, L1157 B1, where CH_3CHO, $HCOOCH_3$, $(CH_3)_2O$, and C_2H_5OH were detected by Arce et al. (2008) and Sugimura et al. (2011). The CH_3CHO/CH_3OH and $HCOOCH_3/CH_3OH$ ratios in L1157 B1 are significantly lower than the ratios in TMC-1 MP. If CH_3OH, CH_3CHO, and $HCOOCH_3$ are supplied from dust grains by sputtering in the shocked region, the CH_3CHO and $HCOOCH_3$ abundances relative to CH_3OH on dust grains in L1157 B1 should be lower than those in TMC-1 MP. L1157 B1 is a shocked region caused by the interaction between an ambient cloud and the molecular outflow from IRAS 20386+6751 (Mikami et al. 1992; Umemoto et al. 1992; Bachiller & Pérez Gutiérrez 1997). Hence, the formation of COMs on dust grains may have not well proceeded in comparison with TMC-1 MP. This implication is consistent with the idea that the abundance of CH_3OH and COMs gradually increases with time (Garrod & Herbst 2006). Alternatively, COMs may be more easily destroyed in the shocked region than CH_3OH, so that their abundances relative to CH_3OH become lower. There is also a possibility that the emitting region of COMs are smaller than that of CH_3OH.

It is worth noting that Requena-Torres et al. (2007) reported the upper limits of the $HCOOCH_3/CH_3OH$ ratio in the quiescent dark cloud L183 and the L1448 outflow. They are not stringent, and are consistent with the TMC-1 MP and L1157 B1 values.

TMC-1 CP is known to be a young starless core, because it harbors rich carbon-chain molecules and deficient NH_3 and HN_2^+ (Hirahara et al. 1992; Kaifu et al. 2004; Sakai & Yamamoto 2013). TMC-1 MP is spatially close to TMC-1 CP, and both are within the starless core, Core D, of Hirahara et al. (1992). The present detection of COMs in such a young starless core is very important. It is most likely that a substantial amount of COMs has already been formed on dust grains even in the early evolutionary stage of starless cores. At the same time, it is found that H_2CCO and cyclopropenone are likely formed in gas-phase processes, as proposed by Loison et al. (2016) and Vasyunin & Herbst (2013). This result means that COMs are not always formed on dust grains. Further theoretical, laboratory, and modeling works are awaited to account for the present observation.

The authors are grateful to Eric Herbst, Cecilia Ceccarelli, and Bertrand Lefloch for valuable discussions. The authors thank the anonymous reviewer for valuable comments. This study is supported by Grant-in-Aids from Ministry of Education, Culture, Sports, Science, and Technologies (25108005, 25400223, 16H03964). The authors acknowledge financial support by JSPS and MAEE under the JapanFrance integrated action program. T.S. thanks the Advanced Leading Graduate Course for Photon Science (ALPS) for financial support.

ORCID iDs

Tatsuya Soma https://orcid.org/0000-0001-6219-7134
Nami Sakai https://orcid.org/0000-0002-3297-4497
Yoshimasa Watanabe https://orcid.org/0000-0002-9668-3592

References

Aikawa, Y., Ohashi, N., Inutsuka, S., Herbst, E., & Takakuwa, S. 2001, ApJ, 552, 639
Arce, H. G., Santiago-García, J., Jørgensen, J. K., Tafalla, M., & Bachiller, R. 2008, ApJL, 681, L21
Bachiller, R., & Pérez Gutiérrez, M. 1997, ApJL, 487, L93
Bacmann, A., & Faure, A. 2016, A&A, 587, A130
Bacmann, A., García-García, E., & Faure, A. 2016, A&A, 588, L8
Bacmann, A., Taquet, V., Faure, A., Kahane, C., & Ceccarelli, C. 2012, A&A, 541, L12
Balucani, N., Ceccarelli, C., & Taquet, V. 2015, MNRAS, 449, L16
Benson, P. J., & Myers, P. C. 1989, ApJS, 71, 89
Bertin, M., Romanzin, C., Doronin, M., et al. 2016, ApJL, 817, L12
Bisschop, S. E., Jørgensen, J. K., van Dishoeck, E. F., & de Wachter, E. B. M. 2007, A&A, 465, 913
Bizzocchi, L., Caselli, P., Spezzano, S., & Leonardo, E. 2014, A&A, 569, A27
Blake, G. A., Sutton, E. C., Masson, C. R., & Phillips, T. G. 1987, ApJ, 315, 621
Bottinelli, S., Ceccarelli, C., Lefloch, B., et al. 2004, ApJ, 615, 354
Caselli, P., Keto, E., Bergin, E. A., et al. 2012, ApJL, 759, L37
Cazaux, S., Tielens, A. G. G. M., Ceccarelli, C., et al. 2003, ApJL, 593, L51
Cernicharo, J., Marcelino, N., Roueff, E., et al. 2012, ApJL, 759, L43
Dickens, J. E., Langer, W. D., & Velusamy, T. 2001, ApJ, 558, 693
Faure, A., Remijan, A. J., Szalewicz, K., & Wiesenfeld, L. 2014, ApJ, 783, 22
Garrod, R. T., & Herbst, E. 2006, A&A, 457, 927
Geppert, W. D., Hamberg, M., Thomas, R. D., et al. 2006, FaDi, 133, 177
Goldreich, P., & Kwan, J. 1974, ApJ, 189, 441
Herbst, E., & Leung, C. M. 1986, ApJ, 310, 378
Herbst, E., & Leung, C. M. 1989, ApJS, 69, 271
Herbst, E., & van Dishoeck, E. F. 2009, ARA&A, 47, 427
Hirahara, Y., Suzuki, H., Yamamoto, S., et al. 1992, ApJ, 394, 539
Imai, M., Sakai, N., Oya, Y., et al. 2016, ApJL, 830, L37
Irvine, W. M., Friberg, P., Kaifu, N., et al. 1989, ApJ, 342, 871
Jimenez-Serra, I., Vasyunin, A. I., Caselli, P., et al. 2016, ApJL, 830, L6
Johnson, D. G., Blitz, M. A., & Seakins, P. W. 2000, PCCP, 2, 2549
Kaifu, N., Ohishi, M., Kawaguchi, K., et al. 2004, PASJ, 56, 69
Langer, W. D., Velusamy, T., Kuiper, T. B. H., et al. 1995, ApJ, 453, 293
Loison, J.-C., Agúndez, M., Marcelino, N., et al. 2016, MNRAS, 456, 4101
Martín-Doménech, R., Muñoz Caro, G. M., & Cruz-Díaz, G. A. 2016, A&A, 589, A107
Matthews, H. E., Friberg, P., & Irvine, W. M. 1985, ApJ, 290, 609
Mikami, H., Umemoto, T., Yamamoto, S., & Saito, S. 1992, ApJL, 392, L87
Müller, H. S. P., Schlöder, F., Stutzki, J., et al. 2005, JMoSt, 742, 215
Öberg, K. I., Bottinelli, S., Jørgensen, J. K., & van Dishoeck, E. F. 2010, ApJ, 716, 825
Potapov, A., Sánchez-Monge, A., Schilke, P., et al. 2016, A&A, 594, A117
Requena-Torres, M. A., Marcelino, N., Jiménez-Serra, I., et al. 2007, ApJL, 655, L37
Sakai, N., Sakai, T., & Yamamoto, S. 2006, PASJ, 58, L15
Sakai, N., & Yamamoto, S. 2013, ChRv, 113, 8981
Schöier, F. L., van der Tak, F. F. S., van Dishoeck, E. F., & Black, J. H. 2005, A&A, 432, 369
Soma, T., Sakai, N., Watanabe, Y., & Yamamoto, S. 2015, ApJ, 802, 74
Spezzano, S., Bizzocchi, L., Caselli, P., Harju, J., & Brünken, S. 2016, A&A, 592, L11
Sugimura, M., Yamaguchi, T., Sakai, T., et al. 2011, PASJ, 63, 459
Suzuki, H., Yamamoto, S., Ohishi, M., et al. 1992, ApJ, 392, 551
Umemoto, T., Iwata, T., Fukui, Y., et al. 1992, ApJL, 392, L83
van der Tak, F. F. S., Black, J. H., Schöier, F. L., Jansen, D. J., & van Dishoeck, E. F. 2007, A&A, 468, 627
Vastel, C., Ceccarelli, C., Lefloch, B., & Bachiller, R. 2014, ApJL, 795, L2
Vasyunin, A. I., & Herbst, E. 2013, ApJ, 769, 34
Watanabe, N., & Kouchi, A. 2002, ApJL, 571, L173
Wisenfeld, L., & Faure, A. 2013, MNRAS, 432, 2573
Yamamoto, S. 2017, Introduction to Astrochemistry: Chemical Evolution from Interstellar Clouds to Star and Planet Formation (Tokyo: Springer Japan)